Topological Dirac nodal-net fermions in AlB_2-type TiB_2 and ZrB_2

Xing Feng,[1] Changming Yue,[2] Zhida Song,[2] QuanSheng Wu,[3,*] and Bin Wen[1,†]

[1]*State Key Laboratory of Metastable Materials Science and Technology, Yanshan University, Qinhuangdao 066004, China*

[2]*Beijing National Laboratory for Condensed Matter Physics, and Institute of Physics, Chinese Academy of Science, Beijing 100190, China*

[3]*Theoretical Physics and Station Q Zurich, ETH Zurich, 8093 Zurich, Switzerland*

(Received 2 May 2017; revised manuscript received 26 November 2017; published 24 January 2018)

Based on first-principles calculations and effective model analysis, a Dirac nodal-net semimetal state is recognized in AlB_2-type TiB_2 and ZrB_2 when spin-orbit coupling (SOC) is ignored. Taking TiB_2 as an example, several topological novel states have been found in this nodal-net structure including triple point, nexus, and nodal link, which are protected by the coexistence of spatial-inversion symmetry and time-reversal symmetry. In addition, linearly and quadratically dispersed two-dimensional surface Dirac points have been identified as getting on the B-terminated and Ti-terminated (001) surfaces of TiB_2, respectively, which are analogous to those of monolayer and bilayer graphene.

DOI: 10.1103/PhysRevMaterials.2.014202

I. INTRODUCTION

Based on the solid band theory, the nodal point represents the point connecting the conduction band and the valence band near the Fermi level. One way to classify nodal points is based on their dimensionality [1–4], which accordingly can be divided into three categories. The first one is zero-dimensional (0D) nodal points, which includes Weyl points [5–10], Dirac points [11–14], triple points [15–17], and other higher degeneracy nodal points [18]. The second one is one-dimensional (1D) nodal-line systems, which includes nodal rings [19,20], nodal chains [2,21], and nodal nets [2]. The third one is two-dimensional (2D) nodal surfaces [22]. A semimetal with such nodal points is called a topological semimetal (TS), such as Weyl semimetal (WSM), Dirac semimetal (DSM), Dirac nodal-line semimetal (DNLSM), nodal-chain semimetal, etc.

The 0D nodal point system has been extensively studied during the past decade, due to its nontrivial topological properties and its exotic transport properties. For example, Dirac semimetals have been predicted to be good candidates for quantum devices because of their massless Dirac fermion properties [11–13,23], Weyl semimetals have chiral anomaly, which leads to a chiral magnetic effect [24,25], i.e., an electric current parallel to an external magnetic field [26–31], and a triple point metals could have topological Lifshitz transitions [15].

Investigations of 1D nodal-line systems have been developing in the last few years, due to their great potential in diverse developments in materials science. A nodal-line system has a nontrivial π Berry phase around the nodal line, which would shift the Landau level index by 1/2 [32,33], and leads to drumhead surface states (SSs) [34,35]. There are many types of nodal-line systems, such as single and multiple Dirac nodal-line (DNL) systems in the absence of spin-orbit coupling (SOC) [4,20,22,36–39], nexus [15,40,41], nodal chain with SOC [2], and other crossing nodal lines [3,21,33,38,42–45]. All the proposed nodal-line systems are protected by crystallographic symmetry. Some are protected by the coexistence of time-reversal symmetry T and spatial-inversion symmetry P, namely, PT symmetry [20,22,37,38]. Some are protected by mirror symmetry or glide symmetry [2,46].

In this work, based on first-principles calculations, we theoretically study a new type of nodal structure, namely nodal net, in two AlB_2-type diborides, TiB_2 and ZrB_2, which present a unique combination of properties such as high bond strengths, high melting points, high thermal conductivities, low electrical resistance, and low work functions, and can be easily synthesized in the laboratory [47–50]. To better understand this complex nodal-net structure, we find it includes four classes of nodal-line structures: A, nodal ring in $k_z = 0$ plane surrounding K point; B, nodal line in three vertical mirror planes σ_{v1}, σ_{v2}, and σ_{v3} (see definition on p. 273 of Ref. [51]); C, nodal line along Γ-A starting from a triple point; D, a single isolated nodal ring at $k_z = 0.5$ plane surrounding A point. Furthermore, class-A and class-B nodal lines will cross at a k point along the Γ-K direction. All three class-B nodal lines in the vertical mirror planes terminate at A point, which is also a termination of the class-C nodal line. So A point is also called a nexus point [40,52], which is the termination of several Dirac line nodes. This nodal-net structure differs from previously reported 0D and 1D nodal structures, which may lead to some new magnetic and electrical transport properties. In addition, the linearly and quadratically dispersed surface Dirac cones are found at the $\bar{K}$ point of the surface BZ for B-terminated and Ti-terminated surfaces of TiB_2, respectively.

This paper is organized as follows. In Sec. II, we elucidate the crystal and electronic structure of TiB_2. In Sec. III, we study the complex nodal-net structure both using first-principles calculations and effective $k \cdot p$ model analysis. In Sec. IV, we study the drumhead surface states both for B-terminated and

*wuq@phys.ethz.ch

†wenbin@ysu.edu.cn

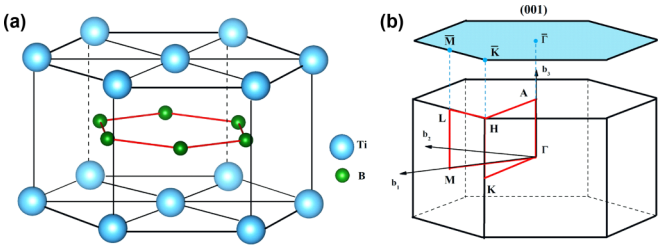

FIG. 1. Crystal structure and Brillouin zone (BZ) of AlB_2-type TiB_2. (a) Crystal structure of AlB_2-type TiB_2 with *P6/mmm* symmetry. Ti atoms occupy the (0.0, 0.0, 0.0) site, and B atoms occupy the (1/3, 2/3, 1/2) site. The optimized lattice constants are $a = b = 3.0335$ Å and $c = 3.2263$ Å. (b) bulk BZ and the projected BZ of the (001) surface.

Ti-terminated surfaces of TiB_2, where linearly and quadratically dispersed surface Dirac points are found.

II. CRYSTAL AND BAND STRUCTURE OF AlB_2-TYPE TiB_2

The crystallographic data of TiB_2 and ZrB_2 are obtained from Ref. [49]. TiB_2 and ZrB_2 have the same AlB_2-type centrosymmetric crystal structures with the space group $P6/mmm$ (191). As verified by calculation, we find that TiB_2 (Fig. 2) and ZrB_2 (Fig. 7) have similar electronic structures, therefore, we take TiB_2 as an example hereafter. As shown in Fig. 1(a), it is a layered hexagonal structure with alternating close-packed hexagonal layers of titanium and graphenelike boron layers. The optimized lattice constants are $a = b = 3.0335$ Å and $c = 3.2263$ Å, which agree well with the experimental [53] and other theoretical [54] results.

To study the electronic properties of TiB_2, the electronic band structure (BS) and projected density of states (PDOS) are calculated in absence of SOC (see details in Appendix A), as shown in Fig. 2(a). It shows that the valence and conduction bands near the Fermi level exhibit Dirac linear dispersion. There are six band crossing points [also called nodal points (NPs)] located along the H-Γ, Γ-A, A-H, K-Γ, M-K, and L-A lines [marked as a to f points in Fig. 2(a)]. It is noticed that these six NPs deviate from the Fermi level about −0.16, 0.5, 0.35, −0.01, −0.28, and 0.32 eV, respectively. To investigate the formation mechanism of these crossing points, orbital-character analysis is performed. As shown in Fig. 2(a), the Ti 3d states in TiB_2 are the dominant feature for these six NPs. Specifically, a is dominated by Ti-d_{xz}, Ti-d_{x2-y2}, and Ti-d_{z2} orbitals; b is dominated by Ti-d_{yz} and Ti-d_{z2} orbitals; c is dominated by Ti-d_{xy}, Ti-d_{yz}, and Ti-d_{x2-y2} orbitals; d is dominated by Ti-d_{xz} and Ti-d_{z2} orbitals; e is dominated by Ti-d_{xz}, Ti-d_{x2-y2}, and Ti-d_{z2} orbitals; f is dominated by Ti-d_{yz} and Ti-d_{x2-y2} orbitals, respectively, as well as, the B atoms' contribution for these six NPs can be ignored [55]. From another perspective, it can also be verified by the calculated charge states around these six NPs, which is shown in Fig. 3. As we can see, the charge states around these six NPs show a inversion feature, and the results agree well with our orbital-character analysis. The Fermi surface (FS) of TiB_2 is calculated and shown in Figs. 2(b) and 2(c), which shows a lanternlike frame with compensated electron pockets and hole pockets, which is a feature of a topological semimetal and also will lead

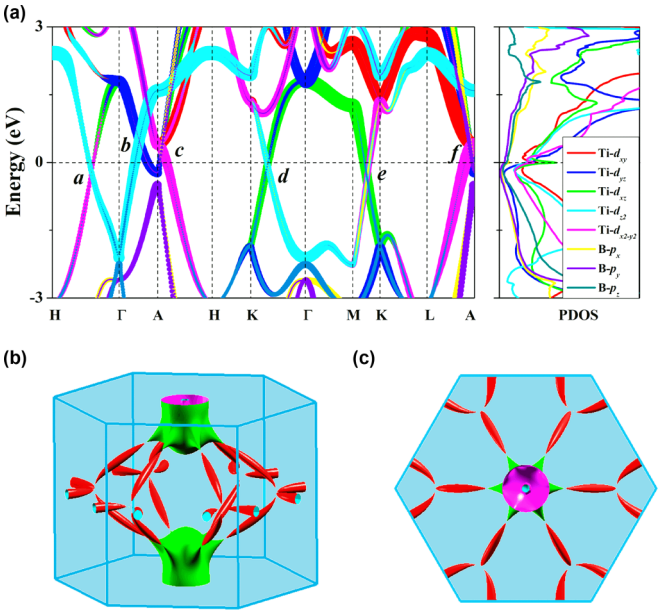

FIG. 2. Electronic energy band and Fermi surface of TiB_2. (a) Fat band of TiB_2. (b) Side view and (c) top view of the Fermi surface of TiB_2.

to nonsaturated large positive magnetoresistance [28]. The FS calculated in this work agrees well with previous experimental [56] and theoretical studies [49].

In presence of the SOC effect, the crossing points along the H-Γ, A-H, K-Γ, M-K, and L-A lines are fully gapped, which is common in PT protected systems [34,38]. SOC makes the crossing points open gaps about 26, 18, 25, 23, and 21 meV (see Fig. 4), respectively. The millivolt level gaps indicated that the effect of SOC on the electronic band structure of TiB_2 is quite weak and can be ignored in experimental work. One thing worth mentioning here is that the SOC splitting would generate a Dirac point along the $\Gamma - A$ direction [Fig. 4(b)], although it happens between the $(N + 2)$th and $(N + 3)$th bands, where N is the number of occupied bands at Γ point in the BZ.

III. NODAL-NET STRUCTURE

From previous studies, we know that a nodal-line system would have banana-shaped linked FSs [57,58] as the NPs do not usually align at the same energy level. In other words, these banana-shape linked FSs are an indication of the existence of

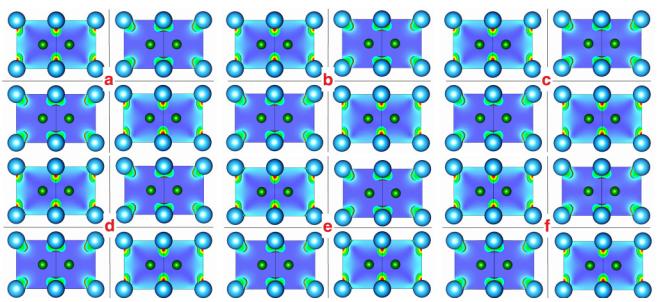

FIG. 3. Charge states of the a, b, c, d, e, and f points in the energy band of AlB_2-type TiB_2 around the Fermi level.

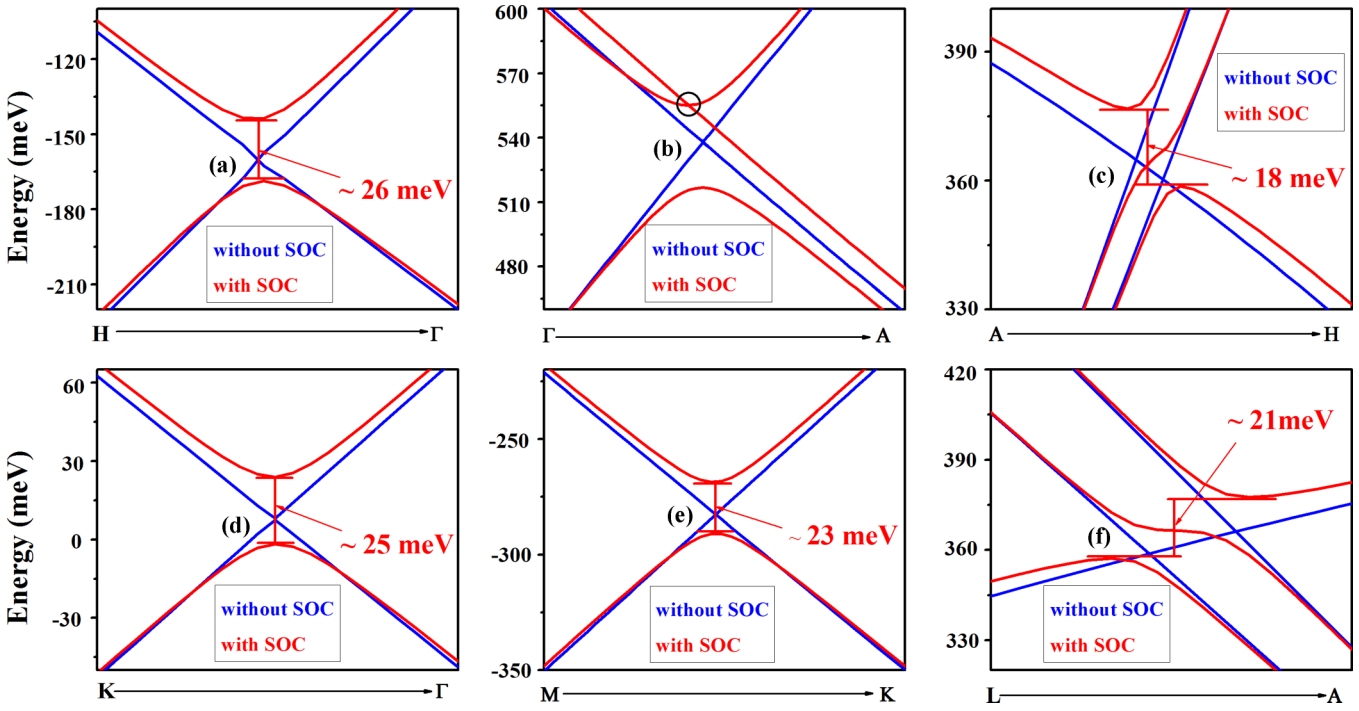

FIG. 4. Comparison between energy bands without SOC and with SOC close to the six nodal points. The triple point along Γ-A in the absence of SOC degenerates to a Dirac point between $(N+2)$th and $(N+3)$th bands, which is marked by a black circle in (b) when SOC is included.

a nodal-line structure. There is another clue to find NLSM for a PT symmetry protected system, i.e., if there is a band touching point close to the Fermi level, there should be a nodal line including this point [34]. Based on these two clues, and the BS and FS shown in Fig. 2, it is clear that there is a nodal-line structure in the TiB_2 system. By using the symmetrical Wannier tight-binding model [15] and WANNIERTOOLS [59], we have found all k points with zero local energy gap between the Nth and $(N+1)$th energy bands, where N is the number of occupied bands at the Γ point, i.e., $\Delta(\mathbf{k}) = E_{N+1}(\mathbf{k}) - E_N(\mathbf{k}) = 0$. The nodal points are plotted in Fig. 5, from which, the energies of nodal points are not the same, which leads to the lanternlike FSs as shown in Fig. 2(b).

TiB_2 has PT symmetry, which is enough to protect the existence of Dirac nodal lines in the absence of SOC. While, besides PT symmetry, there are another four mirror symmetries $\sigma_h, \sigma_{v1}, \sigma_{v2}$, and σ_{v3} in the D_{6h} group. Such mirror symmetries will help to protect the nodal link point. Thus these nodal lines form an interconnected nodal-net structure including four classes of nodal lines: A, B, C, and D. In Appendix, with the aid of DFT calculations, it is verified that class-A, class-B, and class-D nodal lines still exist, but apart from the previous mirror plane, by breaking the mirror symmetries, however, the class-C nodal lines will disappear.

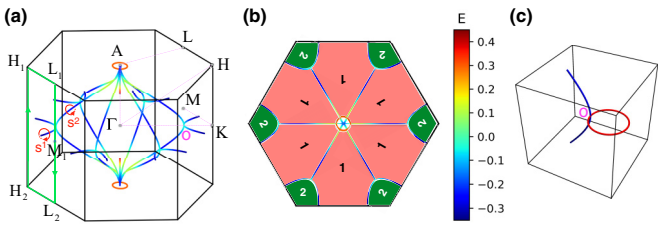

FIG. 5. Nodal-net structure of TiB_2. (a) All nodal points in the first BZ. The color indicates the energy of nodal points with reference to the Fermi energy. Two red arrowed circles and the closed green rectangle are used to calculate the Berry phase. (b) Top view of (a), the topological number v for regions 1 and 2 are 0 and 1, respectively. (c) Sketch view of the nodal link of class-A NL (red) and class-B NL (blue) and O is the nodal link point.

Class-A nodal lines. Those nodal rings surrounding K point are embedded in the $k_z = 0$ plane, which is a mirror plane σ_h of D_{6h}, and is shown as six arcs around K point in Fig. 5. The effective $k \cdot p$ model at K point was constructed within the little group D_{3h}, and is shown in Eq. (D11). When $k_z = 0$, $H_{12} = 0$, which leads to two uncoupled blocks. Those two eigenvalues of each block lead to one upward and one downward parabola. So, if the energies of the two blocks at K point are different, there will be a nodal ring surrounding K point.

Class-B nodal lines. Those Weyl nodes sitting on the vertical mirror planes σ_{v1}, σ_{v2}, and σ_{v3} are shown as edges of the lantern in Fig. 5(a). We could use the effective $k \cdot p$ model at Γ point shown in Eq. (D5) to prove the existence of a nodal line on such k planes. For simplicity, we choose $\sigma_{v1}(\sigma_{xz})$, a mirror perpendicular to the y axis as an example. On this plane, $k_y = 0$, then the eigenvalues of Eq. (D5) are

$$\epsilon_1 = \tfrac{1}{2}(\alpha + \gamma_1 + \gamma_2 + \sqrt{(\alpha + \gamma_1 - \gamma_2)^2 + 8\beta^2}),$$
$$\epsilon_2 = \gamma_1 - \alpha,$$
$$\epsilon_3 = \tfrac{1}{2}(\alpha + \gamma_1 + \gamma_2 - \sqrt{(\alpha + \gamma_1 - \gamma_2)^2 + 8\beta^2}),$$

where $\alpha = Ck_x^2, \beta = Dk_xk_z$, and $\gamma_i = E_i + A_ik_x^2 + B_ik_z^2$ with $i = 1, 2$. At Γ point, $k_x = 0, k_z = 0$, $\epsilon_1 = E_1$, $\epsilon_2 = E_1$, and $\epsilon_3 = E_2$. It is clear that, along $\Gamma - A$, where $k_x = 0$, $\epsilon_1 = \epsilon_2$, which is the evidence of the existence of class-C nodal lines. The nodal line in classes other than class-C could exist only if $\epsilon_1 = \epsilon_3$ or $\epsilon_2 = \epsilon_3$. $\epsilon_1 = \epsilon_3$ would lead to constraint $E_2 - E_1 = Ck_x^2$ and $k_xk_z = 0$, which results in a touching point $k_z = 0, k_y = 0, k_x = \sqrt{(E_2 - E_1)/C}$. However, the DFT fitting results show that $E_2 - E_1 < 0$. So there is no touching point between ϵ_1 and ϵ_3. Another possibility, $\epsilon_2 = \epsilon_3$, would lead to

$$(C^2 + A_2 - A_1)k_x^2 + (B_2 - B_1 - D)k_z^2 = E_1 - E_2. \quad (1)$$

There are three possibilities arising from the relationship between the parameters in Eq. (1), which are the following. (1) If $(C^2 + A_2 - A_1)(E_1 - E_2) > 0$ and $(B_2 - B_1 - D)(E_1 - E_2) > 0$, then there will be an elliptic nodal ring centered at Γ point. (2) If $(C^2 + A_2 - A_1)(B_2 - B_1 - D) < 0$, then there will be a hyperbolic nodal ring. (3) If $(C^2 + A_2 - A_1)(E_1 - E_2) < 0$ and $(B_2 - B_1 - D)(E_1 - E_2) < 0$, there will be no nodal line. According to the DFT fitting parameters, TiB_2 belongs to the first class, which have an elliptical nodal ring on three vertical mirror planes σ_{v1}, σ_{v2}, and σ_{v3}.

Actually, there are three other mirror symmetries σ_{d1}, σ_{d2}, and σ_{d3} in D_{6h}. Take $\sigma_{d1}(\sigma_{yz})$ as an example, we could perform the same analysis above by setting $k_x = 0$, however, we have to admit that the results are the same as in the $k_y = 0$ plane, i.e., there will be a nodal line in the $k_x = 0$ plane. The reason for this is that the $k \cdot p$ model in Eq. (D5) is up to the second order, which will lead to isotopic effects on k_x and k_y. Eventually, there are not only nodal lines in the mirror planes, but also a nodal surface encompassing the Γ point. So, in order to degenerate the nodal surface and distinguish between the $k_x = 0$ and $k_y = 0$ planes, we have to include higher-order terms in the $k \cdot p$ model, as discussed in Appendix D 2.

Nodal link of class-A and class-B NLs. Figure 5(a) shows that the class-A NL is linked with class-B NL at O point along Γ-K direction, which is also shown in Fig. 5(c). Γ-K is the overlap of σ_v and σ_h mirror planes. Eventually, the little group of O is c_{2v} with an additional PT symmetry. The two-band effective $k \cdot p$ model of O up to second order of $\mathbf{k}$ is given as

$$H(k) = \left(M + vk_x + \alpha_1k_x^2 + \alpha_2k_y^2 + \alpha_3k_z^2\right)\sigma_z + \beta k_yk_z\sigma_x, \quad (2)$$

where σ_x and σ_z are Pauli matrices. Since O is a nodal link point, the mass term M should be zero. The eigenvalues of Eq. (2) are

$$E_\pm = \pm\sqrt{\left(vk_x + \alpha_1k_x^2 + \alpha_2k_y^2 + \alpha_3k_z^2\right)^2 + \beta^2k_y^2k_z^2}. \quad (3)$$

The nodal point exists only if $k_yk_z = 0$ and $vk_x + \alpha_1k_x^2 + \alpha_2k_y^2 + \alpha_3k_z^2 = 0$, which leads to two classes of NLs, one is embedded in $k_z = 0$ plane, which belongs to class-A NL, the other one is embedded in $k_y = 0$ plane, which belongs to class-B NL. It is clear that both NLs link together at O. Taking class A as an example, $k_z = 0$, and the other condition becomes $\alpha_1(k_x + \frac{v}{2\alpha_1})^2 + \alpha_2k_y^2 = \frac{v^2}{4\alpha_1}$. It is learned that $v \neq 0$ is the only condition that keeps the NL. $\alpha_1\alpha_2 > 0$ would lead the NL to be elliptic [class-A NL is shown as a red ring in Fig. 5(c)], while $\alpha_1\alpha_2 < 0$ would lead the NL to be hyperbolic [class-B NL is shown as a blue line in Fig. 5(c)]. It is easy to prove that the breaking down of one of the mirror symmetries would only move the nodal link point O and distort the NLs. However, the breakdown of PT symmetry would gap out all nodal points, because σ_y matrix would be introduced to Eq. (2) then. So the nodal link of class-A and class-B NLs are robust under the protection of PT symmetry.

Class-C nodal lines. Actually, such nodal lines are formed by two degenerated bands along the Γ-A direction, which are protected by c_3 symmetry, and shown as a segment between Γ and A points in Fig. 5(a). Along Γ-A, there is another topological fermion, namely, the triple point [15], which is a type-A triple point according to Ref. [15]'s definition, because the Berry phase around Γ-A is zero. Such a triple point would evolve into a Dirac point in the presence of SOC [Fig. 4(b)]. However, the topologically induced SSs of triple points would only happen in a system with SOC, and would not happen in the absence of SOC.

Class-D nodal lines. This is an isolated nodal ring at $k_z = 0$, and is protected by the σ_h mirror symmetry. It is easily deduced from the $k \cdot p$ model [Eq. (D20)]. The eigenvalues of Eq. (D20) are $\epsilon_1^\pm = E_1 + (A \pm C)(k_x^2 + k_y^2)$ and $\epsilon_3^\pm = E_3 + (B_3 \pm G)(k_x^2 + k_y^2)$, since $E_1 < 0$ and $E_3 > 0$, but $(A \pm C) > 0$ and $(B_3 + G) * (B_3 - G) < 0$, $\epsilon_1^\pm$ would have a cross-point with $\epsilon_3^\pm$ due to its typical band inversion. The resulting nodal line is shown as an orange circle at the top plane of Fig. 5(a).

Topological number for the nodal net. The topological number of DNL is characterized by a quantized $\mathbb{Z}_2$ topological charge ν [38], which is given by the parity of the Berry phase along a loop S that interlinks with the Dirac ring [red loop in Fig. 5(a)]. It is verified that ν is 1 for red loops S^1 and S^2. The topological charge ν of red loops S^1 is identical to the topological charge of the green circle in Fig. 5(a), which is composed of lines H_2-H_1, H_1-L_1, L_1-L_2, and L_2-H_2. Due to the mirror symmetry, the summation of Berry phases along H_1-L_1 and L_2-H_2 is zero. We could define a topological charge ν_H and ν_L for H_2-H_1 and L_1-L_2, respectively, since they form a closed loop in k-space. From previous studies [38], the topological number ν for a time reversal invariant loop which links two parity-invariant momenta Γ_a and Γ_b is related to the parity of Γ_a and Γ_b as

$$(-1)^\nu = \xi_a\xi_b; \xi_a = \prod_n \xi_n(\Gamma_a), \quad (4)$$

where $\xi_n(\Gamma_a)$ is the parity for the occupied bands.

So $(-1)^{\nu_L} = \xi_{M_1}\xi_{L_1}$. Since closed loop L_1-L_2 links M_1 and L_1, which are the parity-invariant momenta, it is verified by DFT calculations that $\xi_{M_1} = 1$ and $\xi_{L_1} = 1$ (see details in Appendix E, i.e., $\nu_L = 0$). So the topological number for H_2-H_1 is $\nu_H = (\nu_{S^1} - \nu_L) \bmod 2 = 1$. Eventually, the topological numbers are $\nu = 0$ and 1 for regions 1 and 2 shown in Fig. 5(b) with different colors respectively. There will be an odd number of nodal lines between regions 1 and 2 due to the topological number change from 0 to 1.

IV. DRUMHEAD SURFACE STATES

Based on previous studies [3,38,60], the 1D $\mathbb{Z}_2$ invariant ν partially guarantees the presence of drumhead surface states.

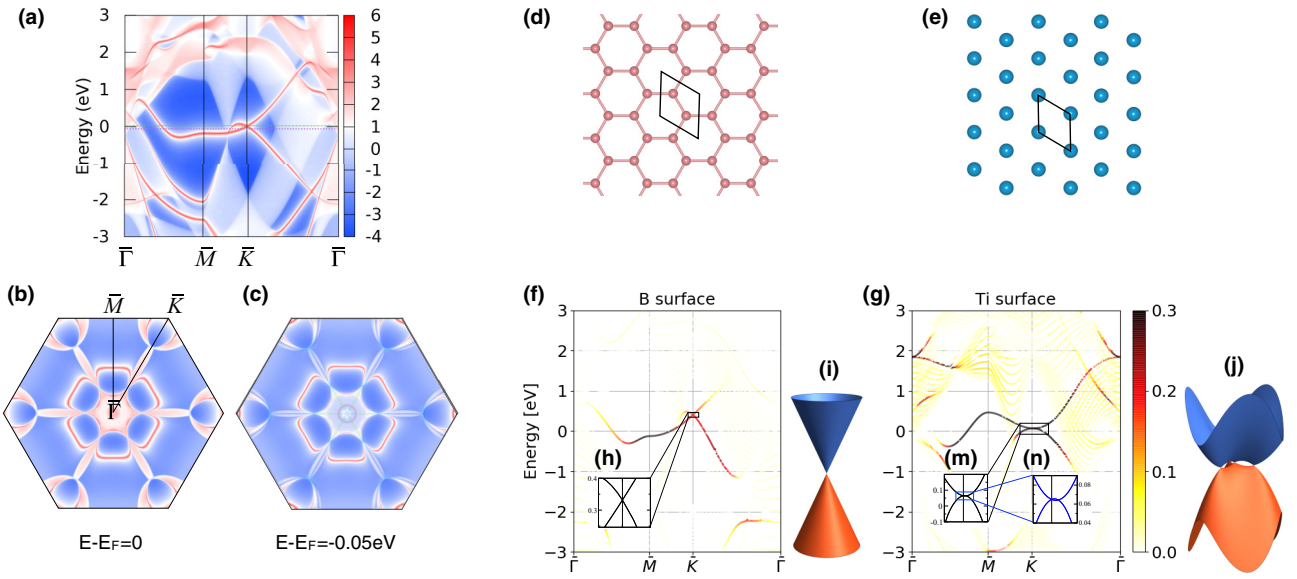

FIG. 6. Surface states analysis of the TiB_2 (001) surface. (a) B-terminated surface-state spectrum calculated from the Wannier TB model. The dashed lines are indicative of $E - E_F = 0$ and $E - E_F = -0.05$ eV. (b) and (c) Surface spectrum at fixed energies $E - E_F = 0$ and $E - E_F = -0.05$ eV, which are shown in a subplot. (d) and (e) show the surface structure for B-terminated and Ti-terminated surfaces, respectively. (g) shows the surface atom weighted band structure, which is calculated from VASP for 20 layers of TiB_2 with Ti(B) sitting in the outer layer.

In this section, the drumhead surface states on B-terminated and Ti-terminated (001) cleavage surfaces of TiB_2 are studied.

The B-terminated surface structure is shown in Fig. 6(d), which is a honeycomb lattice like graphene. By using WANNIERTOOLS [59] and the method of iterative Green's function [61] solution based on a tight-binding model (TBM), the surface state spectrum was calculated, as shown in Figs. 6(a)–6(c). In Fig. 6(a), it is shown that between $\bar{M}$-$\bar{K}$ there is a drumhead surface state coming from a "Dirac" point, which is the projection of the nodal line. In region 1, those drumhead surface states form a linear Dirac cone at $\bar{K}$ point, which is analogous to the Dirac cone in graphene. SSs obtained from the TB model are usually used to explain the topological properties. To compare the SS with ARPES experimental data for further use, we use a first-principles calculations for a slab system due to the fact that a real surface system would have charge reconstructions which cannot be described by TBM. So we simulated a 20-layer slab of TiB_2 with VASP. The BS is shown in Fig. 6(f), in which the color denotes the contributions from the p_z orbital of the surface's boron atoms. Basically, the DFT results are close to the TBM results. The difference is that the zero-energy point of the surface Dirac cone of DFT results is about 0.45 eV higher than that of the TBM results. Since the lattice and the orbital of the boron surface are the same as that of graphene, the effective $k \cdot p$ models at $\bar{K}$ point are the same, and are given as

$$H(\mathbf{k}) = V_F(k_x\sigma_x + k_y\sigma_y), \tag{5}$$

where V_F is the Fermi velocity. By fitting the DFT calculations, V_F is estimated to be 1.5 eVÅ, which is about 2.28×10^5 m/s in SI units.

The Ti-terminated surface structure is shown in Fig. 6(e), which is a hexagonal lattice of the titanium atom. The DFT calculated BS of a 20-layer slab of TiB_2 with titanium in the outer surface is shown in Fig. 6(g), in which the color denotes contributions from d_{zx},d_{yz} orbitals of the surface's titanium atoms. There are drumhead SSs coming from the nodal line, which in this case are same as the B-terminated surface; however, the dispersion of SS at $\bar{K}$ is different from that of B-terminated surface. In Fig. 6(m), it seems that there is a 2D quadratic dispersed Dirac cone at $\bar{K}$ point. However, by zooming into the dispersion at $\bar{K}$ point in Fig. 6(n), it turns out that it is a fake quadratic Dirac cone. Not only there is a linearly dispersed Dirac cone at $\bar{K}$ point, but also a linearly dispersed Dirac cone along $\bar{K}$-$\bar{\Gamma}$. Regarding the point group C_{3v} describing the surface structure, the effective $k \cdot p$ model is obtained as

$$H(\mathbf{k}) = \begin{pmatrix} Bk^2 & Ak_+ + Ck_-^2 \\ Ak_- + Ck_+^2 & Bk^2 \end{pmatrix}, \tag{6}$$

where $k_\pm = k_x \pm ik_y$ and $k^2 = k_x^2 + k_y^2$. When the quadratic terms B and C are missing, then Eq. (6) reduces to Eq. (5), which leads to massless linear Dirac dispersion $E(k) = \pm|k|$. In the absence of linear term A, Eq. (6) describes a Dirac point with parabolic energy dispersion. Such a quadratic Dirac point is unstable due to its topological number ν being trivial. It will split into four linear Dirac points with nontrivial topological number $\nu = 1$ under the C_3 symmetry [40], which leads to the linear term in Eq. (6). Eventually, one is centered at $\bar{K}$ point, the other three are connected by the C_3 symmetry [see Fig. 6(j)]. Fitting to the DFT calculated BS, we obtain the following parameters for a Ti-terminated surface: $A = 0.08$ eV Å, $B = -0.46$ eV Å^2, and $C = 2.3$ eV Å^2, in which the linear term is much weaker than the quadratic term.

The surface Dirac cone at $\bar{K}$ of TiB_2 with B-terminated and Ti-terminated surfaces is very similar to monolayer and bilayer

graphene, which have linearly dispersed and quadratically dispersed Dirac cones, respectively. The Berry phase around the linear Dirac cone is π, while the Berry phase around the quadratically dispersed Dirac cone is 2π. Such differences in the Berry phase would lead to different quantum oscillations. In Ref. [62], it was proposed that a Dirac point could be observed in monolayer TiB_2; however, the Dirac point proposed in this paper could be observed on the surface of a thick slab system rather than a monolayer system.

V. CONCLUSION

In this paper, based on first-principles calculations and model analysis, a novel PT symmetry protected Dirac nodal-net state is recognized in AlB_2-type TiB_2 and ZrB_2 in the absence of SOC. This complex nodal-net structure is composed of four classes of NLs: A, B, C, and D, in which, class-A and class-B NLs link together at O along the Γ-K direction, three class-B NLs in the vertical mirror planes terminate at A point, which is also a termination of the class-C NL. Several $k \cdot p$ models for these four classes of NLs are constructed under the constraint of their symmetry, which confirmed the formation of this nodal net. The topological numbers ν for different regions in BZ are calculated. It is noted that there are two different dispersed drumheadlike Dirac cones emerging on B-terminated and Ti-terminated surfaces, which are analogous to those of monolayer and bilayer graphene, indicating some novel surface transport properties in TiB_2 and ZrB_2. We believe that this work will guide further progress in understanding the novel properties of TiB_2 and ZrB_2, and two different terminated surfaces are good platforms to study 2D Dirac fermions. In addition, AlB_2-type TiB_2 and ZrB_2 can be easily synthesized and provide two prototype materials to study the topological nodal-net structure.

Note added. Recently, Ref. [63] appeared, discussing some of the topological properties of metal-diboride where the nodal line around K is the class-A nodal line in the nodal net of this work.

ACKNOWLEDGMENTS

We acknowledge helpful discussions with X. Dai. X.F. and B.W. were supported by the National Natural Science Foundation of China (NSFC-51372215, NSFC-51771165, and NSFC-51372215), C.Y. and Z.S. were supported by National Natural Science Foundation of China, the National 973 program of China (Grant No. 2013CB921700), Q.W. was supported by Microsoft Research, and the Swiss National Science Foundation through the National Competence Centers in Research MARVEL and QSIT.

X.F. and C.M.Y. contributed equally to this work.

APPENDIX A: COMPUTATIONAL METHODS

In this work, the electronic properties for AlB_2-type TiB_2 are studied by using density functional theory (DFT) [64,65] as implemented in the Vienna *ab initio* simulation package (VASP) [66–68]. The exchange correlation functional of Perdew-Burke-Emzerhof generalized gradient approximation (GGA-PBE) [69,70] is used in the calculations. The standard version of PBE pseudopotential is adopted in this work explicitly treating four valence electrons for the Ti atoms ($3d^3 4s^1$) and three valence electrons for the B atoms ($2s^2 2p^1$). A cutoff energy of 500 eV and a $11\times11\times9$ k mesh are used to perform the bulk calculation. The conjugate-gradient algorithm is used to relax the ions, and the convergence thresholds for total energy and ionic force component are chosen as 1×10^{-7} eV and 0.001 eV/Å.

For the slab calculations [Figs. 6(f) and 6(g)], the thickness of the B-terminated slab is 20 layers of titanium and 21 layers of boron, while the thickness of the Ti-terminated slab is 20 layers of titanium and 19 layers of boron. A $26 \times 26 \times 1$ Γ-centered k mesh and a 14-Å-thick vacuum are used in the DFT simulations. The surface is fully relaxed with energy convergence up to 1×10^{-7} eV and a force up to 0.001 eV/Å.

The nodal-net searching and surface states spectrum calculations shown in Figs. 6(a)–6(c) are done using the open-source software WANNIERTOOLS [59], which is based on the Wannier tight-binding model (WTBM) constructed with WANNIER90 [71]. Ti s, p, d, and B s, p orbitals are used as initial projectors for WTBM construction. WTBMs constructed with WANNIER90 do not exactly fulfill all crystal symmetries, which is very important for nodal point searching because usually nodal points are protected by crystal symmetries except Weyl points. The WTBM is symmetrized to be compatible with the crystal symmetry using the method described in Ref. [15].

APPENDIX B: BAND STRUCTURE AND FERMI SURFACE OF AlB_2-TYPE ZrB_2

In general, ZrB_2 is often compared with TiB_2. The structure of AlB_2-type ZrB_2 also has hexagonal structure with a space group of $P6/mmm$ (No. 191). Its optimized lattice constants are $a = b = 3.1748(3)$ Å and $c = 3.5579(7)$ Å, which are slightly larger than those of TiB_2. As shown in Fig. 7(a), there

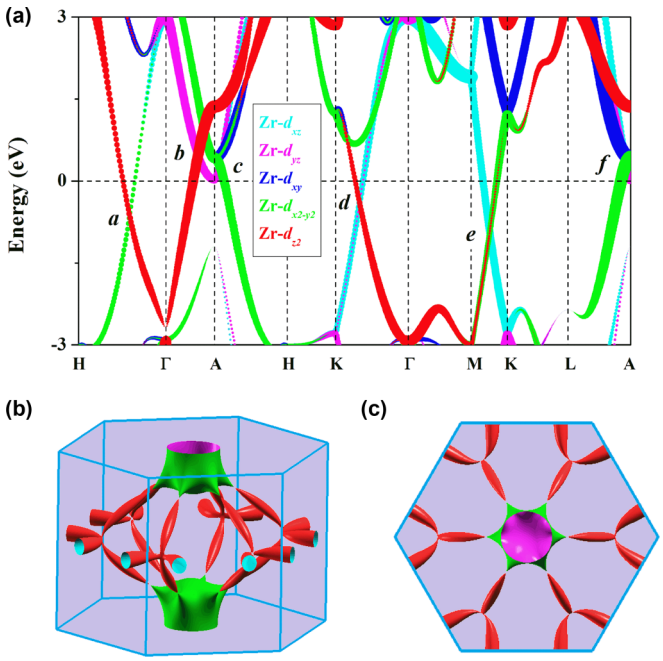

FIG. 7. Electronic energy band and Fermi surface of AlB_2-type ZrB_2. (a) Fat band of AlB_2-type ZrB_2. (b) Side view and (c) top view of the Fermi surface of AlB_2-type ZrB_2.

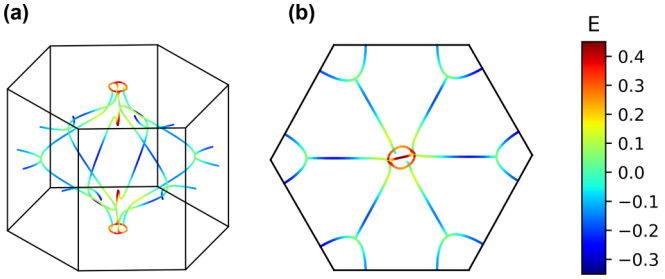

FIG. 8. Nodal-net structure of TiB_2 without vertical mirror planes.

are also six band crossing points along the high-symmetry path similar with TiB_2. Among them, Zr $4d$ states are the main contributing orbitals for these six band crossing points. The Zr-d_{xz} and Zr-d_{xy} orbitals are much higher than the Fermi level. From Figs. 7(b) and 7(c), the Fermi surface of ZrB_2 is sightly different from that of TiB_2. The circling surface around A point disappeared in the Fermi surface of ZrB_2. The main part of the lanternlike Fermi surface of ZrB_2 is basically consistent with the Fermi surface of TiB_2, which also shows a nodal-net feature.

APPENDIX C: NODAL-NET STRUCTURE OF TiB_2 WITHOUT VERTICAL MIRROR PLANES

Since the nodal net of TiB_2 is PT symmetry protected, any perturbations that preserve the inversion symmetry can only distort the nodal-net but not destroy them. As an example,we apply a uniaxial strain (compression 1%) along the [100] crystal direction. After deformation, the structure of AlB_2-type TiB_2 belongs to space group of $C2/m$ (No. 12), which just preserves the M_z mirror reflection symmetry. As a result, as shown in Fig. 8, it is found that the class-A nodal line is still embedded in the $k_z = 0$ plane, one of the class-B nodal line becomes isolated with the other two class-B nodal lines, which link with the class-D nodal line that is embedded in the $k_z = 0.5$ plane, while the class-D nodal line along Γ-A disappears because it is protected by C_3 symmetry, which is destroyed under such strain. Thus the nodal net in TiB_2 is robustly stable, which does not require the protection of mirror symmetry.

APPENDIX D: EFFECTIVE $k \cdot p$ MODEL

We derive several $k \cdot p$ models describing the bulk bands in the vicinity of Γ, A, and K in the 3D BZ, and a $k \cdot p$ for the surface states at $\bar{K}$ point in 2D BZ. The $k \cdot p$ models are used to get a better understanding of the surface states and the nodal-net structures, and would be useful for further investigations of Landau level and quantum transport properties.

The $k \cdot p$ models were calculated using the kdotp_symmetry code, which implements the method described in Ref. [72]. Basically, there are two things that should be prepared before applying kdotp_symmetry. Firstly, we identify the little group G of a high symmetry point K_0 of which we want to construct a low-energy effective model, and get the generators R of little group G. Secondly, we identify the representations of R on the basis of the eigenvectors at the selected high-symmetry points. Then, $k \cdot p$ symmetry will produce the $k \cdot p$ model under the constraint

$$D(R)H(k)D^{\dagger}(R) = H(R(k)), \tag{D1}$$

where $D(R)$ is the representative matrix of symmetry operator R.

1. $k \cdot p$ model at Γ point

The little point group at Gamma point of bulk TiB_2 is D_{6h} plus TR symmetry (see Table 76 of Ref. [73]). There are three generators of D_{6h} including spatial-inversion $I(-x, -y, -z)$, twofold rotation $c_{2y}(-x, y, -z)$, and sixfold rotation $c_{6z}(\frac{x}{2} + \frac{\sqrt{3}}{2}y, -\frac{\sqrt{3}}{2}x + \frac{y}{2}, z)$. From the fat-band analysis of Fig. 2, the relevant bands come from d_{z^2}, which belongs to the A_{1g} representation, d_{zx} and d_{yz} orbitals, which form the basis of its E_{1g} representation. The representations of group generators according to the symmetrical basis $\{(d_{zx} + id_{yz})/\sqrt{2}, (d_{zx} - id_{yz})/\sqrt{2}, d_{z^2}\}$ are given by

$$D(I) = \mathrm{diag}\{1,1,1\},$$
$$D(c_{6z}) = \mathrm{diag}\{-e^{i2\pi/3}, -e^{-i2\pi/3}, 1\}, \tag{D2}$$

$$D(c_{2y}) = \begin{pmatrix} 0 & 1 & 0 \\ 1 & 0 & 0 \\ 0 & 0 & 1 \end{pmatrix}, \tag{D3}$$

$$D(\mathrm{TR}) = \begin{pmatrix} 0 & 1 & 0 \\ 1 & 0 & 0 \\ 0 & 0 & 1 \end{pmatrix} K, \tag{D4}$$

where K is the complex conjugation operator. Considering these symmetries, and the constraint of Eq. (D1), a three-band model up to second order of k around Γ point for bulk TiB_2 is given by

$$H(\mathbf{k}) = \begin{pmatrix} \varepsilon_1(\mathbf{k}) & Ck_-^2 & Dk_-k_z \\ Ck_+^2 & \varepsilon_1(\mathbf{k}) & Dk_+k_z \\ Dk_+k_z & Dk_-k_z & \varepsilon_2(\mathbf{k}) \end{pmatrix}, \tag{D5}$$

where $\varepsilon_1(\mathbf{k}) = E_1 + A_1(k_x^2 + k_y^2) + B_1k_z^2$ and $\varepsilon_2(\mathbf{k}) = E_2 + A_2(k_x^2 + k_y^2) + B_2k_z^2$.

As mentioned in the main text, Eq. (D5) with only second-order momentum k would lead to a nodal surface other than the nodal-line structure. To distinguish the difference between Γ-K and Γ-M directions, we have to introduce the sixth order of k_x, k_y in the $k_z = 0$ plane, and introduce a fourth order of k_x, k_y in the off-diagonal part, so eventually, the new $k \cdot p$ model is given by

$$H(\mathbf{k}) = \begin{pmatrix} \varepsilon_1(\mathbf{k}) & Ck_-^2 + Fk_+^4 & Dk_-k_z \\ Ck_+^2 + Fk_-^4 & \varepsilon_1(\mathbf{k}) & Dk_+k_z \\ Dk_+k_z & Dk_-k_z & \varepsilon_2(\mathbf{k}) \end{pmatrix}, \tag{D6}$$

where $\varepsilon_1(\mathbf{k}) = E_1 + A_1(k_x^2 + k_y^2) + B_1k_z^2$ and $\varepsilon_2(\mathbf{k}) = E_2 + A_2(k_x^2 + k_y^2) + B_2k_z^2 + L(k_x^2 + k_y^2)^2 + M(k_+^6 + k_-^6)$.

By fitting the value to the DFT band structure of TiB_2, the parameters in Eq. (D6) are obtained: $E_1 = 1.787\,\mathrm{eV}$, $B_1 = -3.8\,\mathrm{eV\AA}^2$, $A_1 = 2.6\,\mathrm{eV\AA}^2$, $E_2 = -2.12\,\mathrm{eV}$, $A_2 = 1.63\ \mathrm{eV\AA}^2$, $B_2 = 5.1\ \mathrm{eV\AA}^2$, $L = 1.3\ \mathrm{eV\AA}^4$, $C = 3.55\ \mathrm{eV\AA}^2$, $M = 0.65\ \mathrm{eV\AA}^6$, $F = 1.83\ \mathrm{eV\AA}^4$, and $D =$

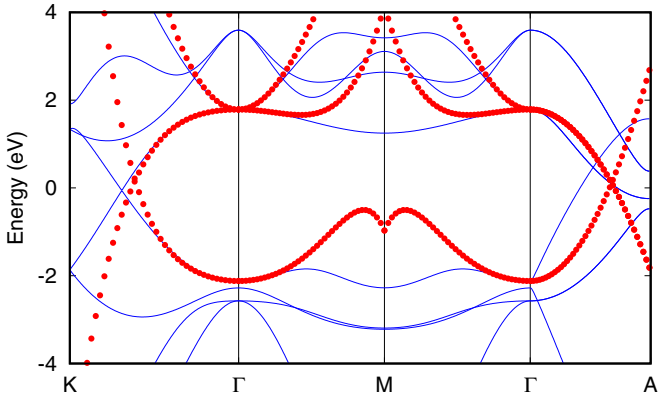

FIG. 9. Comparison between DFT bands and the bands from the $k \cdot p$ model [Eq. (D6)] at Γ point of TiB_2. Blue lines come from DFT calculations and red dotted lines come from $k \cdot p$ model.

5.1 eVÅ^2. The comparison between DFT bands and $k \cdot p$ bands is shown in Fig. 9

The nodal-line structure around Γ point calculated from Eq. (D6) with the DFT fitted parameters is shown in Fig. 10(a). It is shown that the nodal net close to the Γ point is very similar to Fig. 3, the class-A, class-B, and class-C nodal lines are captured successfully; however, the nodal line beyond the nexus point A is not captured. This is because the nexus point A is at the boundary of the BZ, which is related to an infinity in the $k \cdot p$ model. The position of the nexus point A could be tuned by changing F in Eq. (D6). In Fig. 10(c), it is shown that the nexus point would have disappeared if F was very large. The nodal line in the σ_d mirror plane could be shown if the fourth and sixth order terms in Eq. (D6) become smaller [Fig. 10(b)].

2. $k \cdot p$ model at K point

The little group at K point in the TiB_2 is D_{3h} (see Table 65 of Ref. [73]), of which there are three generators including horizontal mirror $\sigma_h(x, y, -z)$, twofold rotation $c_{2x}(x, -y, -z)$, and threefold rotation $c_{3z}(-\frac{x}{2} - \frac{\sqrt{3}}{2}y, \frac{\sqrt{3}}{2}x - \frac{y}{2}, z)$. Around K point, the relevant representations are Γ_5 and Γ_6, of which the basis are $\{d_{zx}, d_{yz}\}$ and $\{d_{xy}, d_{x^2-y^2}\}$. Taking the symmetrical orbitals $\{|Y_2^1\rangle, -|Y_2^{-1}\rangle\}$ and $\{-|Y_2^2\rangle, |Y_2^{-2}\rangle\}$ as a basis,

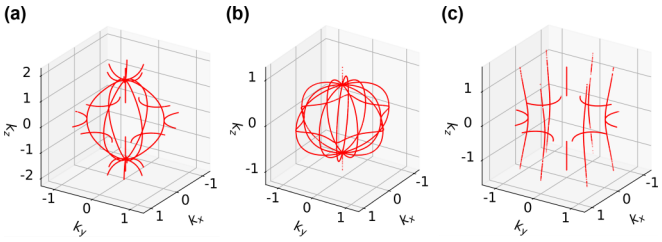

FIG. 10. Nodal-line structure obtained from Eq. (D6) at Γ point of TiB_2 with different M, F, and D parameters. (a) $M = 0.65$ eVÅ^6, $F = 1.83$ eVÅ^4, and $D = 5.1$ eVÅ^2. (b) $M = 0$, $F = 1.18$ eVÅ^4, and $D = 2.53$ eVÅ^2. (c) $M = 0.65$ eVÅ^6, $F = 7.6$ eVÅ^4, and $D = 5.1$ eVÅ^2.

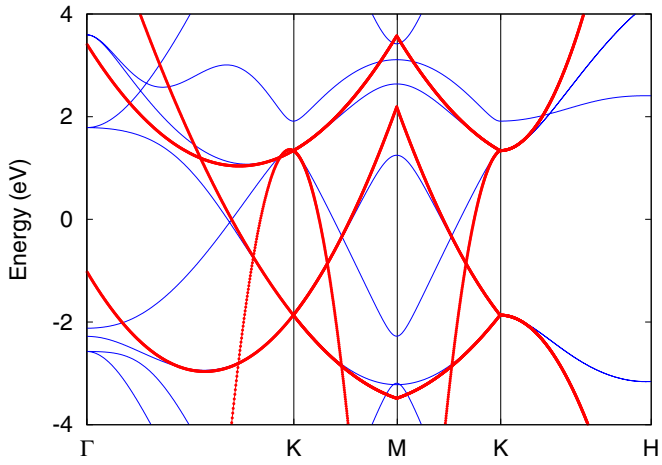

FIG. 11. Comparison between DFT bands and the bands from the $k \cdot p$ model [Eq. (D10)] at K point of TiB_2. Blue lines come from DFT calculation, and red dotted lines come from $k \cdot p$ model.

where $|Y_l^m\rangle$ is the complex spherical harmonic function, the representations of the generators are given by

$$D(\sigma_h) = \mathrm{diag}\{-1, -1\} \oplus \mathrm{diag}\{1, 1\}, \tag{D7}$$

$$D(c_{2x}) = \begin{pmatrix} 0 & -1 \\ -1 & 0 \end{pmatrix} \oplus \begin{pmatrix} 0 & -1 \\ -1 & 0 \end{pmatrix}, \tag{D8}$$

$$D(c_{3z}) = \begin{pmatrix} e^{-2i\pi/3} & 0 \\ 0 & e^{2i\pi/3} \end{pmatrix} \oplus \begin{pmatrix} e^{2i\pi/3} & 0 \\ 0 & e^{-2i\pi/3} \end{pmatrix}. \tag{D9}$$

Considering the above symmetries and the constraint of Eq. (D1), a four-band model up to second order of k around K point in bulk TiB_2 is given by

$$H(k) = \begin{pmatrix} \varepsilon(k) & Ck_+ + Dk_-^2 & iEk_zk_+ & Fk_z \\ Ck_- + Dk_+^2 & \varepsilon(k) & Fk_z & -iEk_zk_- \\ -iEk_zk_- & Fk_z & \varepsilon'(k) & C'k_- + D'k_+^2 \\ Fk_z & iEk_zk_+ & C'k_+ + D'k_-^2 & \varepsilon'(k) \end{pmatrix}, \tag{D10}$$

where $\varepsilon(k) = E_0 + A(k_x^2 + k_y^2) + Bk_z^2$ and $\varepsilon'(k) = E_0' + A'(k_x^2 + k_y^2) + B'k_z^2$. The fitted parameters of TiB_2 are $E_0 = -1.8651$ eV, $E_0' = 1.3387$ eV, $A = 2.55$ eVÅ^2, $A' = -16.5$ eVÅ^2, $C = 3.7$ eVÅ, $C' = -1.66$ eVÅ, $D = -0.58$ eVÅ^2, $D' = 18.8$ eVÅ^2, $B = 8.73$ eVÅ^2, $B' = -6.37$ eVÅ^2, $E = 24.9$ eVÅ^2, and $F = 6.84$ eVÅ. The comparison between DFT bands and $k \cdot p$ bands is shown in Fig. 11.

In order to analyze the nodal-line structure, Eq. (D10) can be written into two blocks:

$$H(k) = \begin{pmatrix} H_{11} & H_{12} \\ H_{12}^\dagger & H_{22} \end{pmatrix}, \tag{D11}$$

where

$$H_{11} = \begin{pmatrix} \varepsilon(k) & Ck_+ + Dk_-^2 \\ Ck_- + Dk_+^2 & \varepsilon(k) \end{pmatrix}, \tag{D12}$$

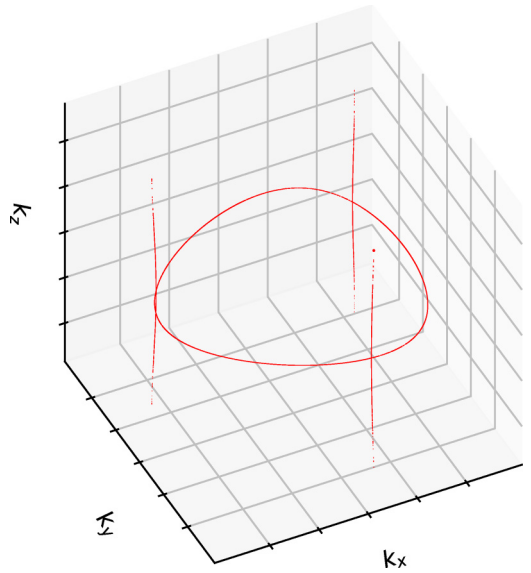

FIG. 12. Nodal-line structures close to K point calculated from the $k \cdot p$ model [Eq. (D10)]. The coordinates are relative to the K point.

$$H_{22} = \begin{pmatrix} \varepsilon'(k) & C'k_+ + D'k_-^2 \\ C'k_- + D'k_+^2 & \varepsilon'(k) \end{pmatrix}, \quad \text{(D13)}$$

$$H_{12} = \begin{pmatrix} iEk_zk_+ & Fk_z \\ Fk_z & -iEk_zk_- \end{pmatrix}. \quad \text{(D14)}$$

With the fitted parameters, we find that our $k \cdot p$ model not only describes the nodal line surrounding the K point, but can also predict part of the nodal line in the vertical mirror plane as shown in the Fig. 12.

3. $k \cdot p$ model at A point

For the little group at A D_{6h} (see Table 76 of Ref. [73]), relevant representations are A_{1g}, E_{1g}, and E_{2g}, which constitutes $\{d_{z^2}\}$, $\{d_{zx}, d_{yz}\}$, and$\{d_{xy}, d_{x^2-y^2}\}$. By symmetrization of those orbitals according to the D_{6h} group, the symmetrical basis are chosen as $|Y_2^0\rangle$, $|Y_2^1\rangle$, $-|Y_2^{-1}\rangle$, $-|Y_2^2\rangle$, and $|Y_2^{-2}\rangle$, and the related representations of its generators are given by

$$D(I) = \mathrm{diag}\{1,1,1,1,1\}, \quad \text{(D15)}$$

$$D(c_{2y}) = 1 \oplus \begin{pmatrix} 0 & 1 \\ 1 & 0 \end{pmatrix} \oplus \begin{pmatrix} 0 & -1 \\ -1 & 0 \end{pmatrix}, \quad \text{(D16)}$$

$$D(c_{6z}) = \mathrm{diag}\{1, -e^{2i\pi/3}, -e^{-2i\pi/3}, e^{-2i\pi/3}, e^{2i\pi/3}\}, \quad \text{(D17)}$$

$$D(\mathrm{TR}) = 1 \oplus \begin{pmatrix} 0 & 1 \\ 1 & 0 \end{pmatrix} \oplus \begin{pmatrix} 0 & -1 \\ -1 & 0 \end{pmatrix} K. \quad \text{(D18)}$$

The constructed $k \cdot p$ model is given by

$$H(k) = \begin{pmatrix} \varepsilon_2(k) & Dk_zk_+ & Dk_zk_- & Ek_+^2 & -Ek_-^2 \\ Dk_zk_- & \varepsilon_1(k) & Ck_-^2 & Fk_zk_+ & 0 \\ Dk_zk_+ & Ck_+^2 & \varepsilon_1(k) & 0 & -Fk_zk_- \\ Ek_-^2 & Fk_zk_- & 0 & \varepsilon_3(k) & Gk_+^2 \\ -Ek_+^2 & 0 & -Fk_zk_+ & Gk_-^2 & \varepsilon_3(k) \end{pmatrix}, \quad \text{(D19)}$$

where $\varepsilon_i(k) = E_i + A_i(k_x^2 + k_y^2) + B_ik_z^2$ with $i = 1,2,3$. The fitted parameters are $E_1 = -0.2426$ eV, $A_1 = 170$ eVÅ^2, $B_1 = 3.53$ eVÅ^2, $E_2 = 1.575$ eV, $A_2 = 1.27$ eVÅ^2, $B_2 = -6.16$ eVÅ^2, $E_3 = 0.3822$ eV, $A_3 = -2.39$ eVÅ^2 $B_3 = 26.55$ eVÅ^2, $C = 0.47$ eVÅ^2, $D = 0.0$, $E = 0.0$, $F = 0.1$ eVÅ^2, and $G = 5.62$ eVÅ^2. The fitted band is shown in Fig. 13.

Particularly, when the effective $k_z = 0$, this means that bulk $k_z = 0.5$, Eq. (D19) decouples into three block-diagonal matrices. From Fig. 2, it is shown that along $A - H$, band crossing happens between d_z^2 and the combination of d_{xz} and d_{yz}, i.e., we only have to consider the following block of Eq. (D19):

$$H(k) = \begin{pmatrix} \varepsilon_1(k) & Ck_-^2 & 0 & 0 \\ Ck_+^2 & \varepsilon_1(k) & 0 & 0 \\ 0 & 0 & \varepsilon_3(k) & Gk_+^2 \\ 0 & 0 & Gk_-^2 & \varepsilon_3(k) \end{pmatrix}. \quad \text{(D20)}$$

4. $k \cdot p$ model for surface states at $\bar{K}$ points

The little group at $\bar{K}$ point of the slab system TiB_2 is C_{3v}, which has two generators $c_{3z}(-\frac{x}{2} - \frac{\sqrt{3}}{2}y, \frac{\sqrt{3}}{2}x - \frac{y}{2}, z)$ and $\sigma_v(x, -y, z)$. According to the DFT calculations, it was determined that the surface state at $\bar{K}$ belongs to E (see Table 49 of Ref. [73]) representation of C_{3v}. On the basis of complex orbitals, the related representations of its generators are given

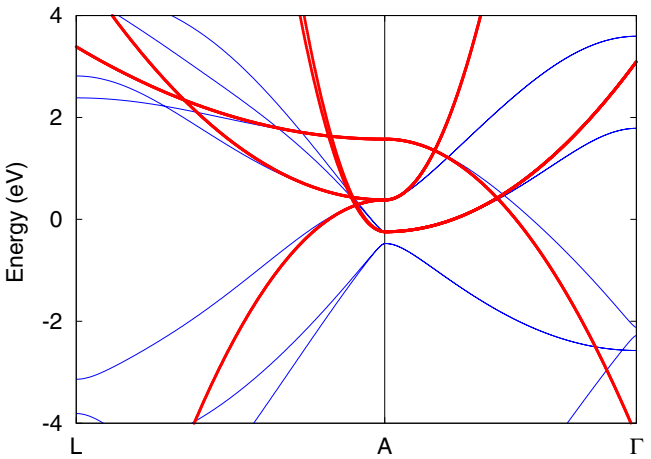

FIG. 13. Comparison between DFT bands and the bands from the $k \cdot p$ model [Eq. (D19)] at A point of TiB_2. Blue lines come from DFT calculations, and red dotted lines come from the $k \cdot p$ model.

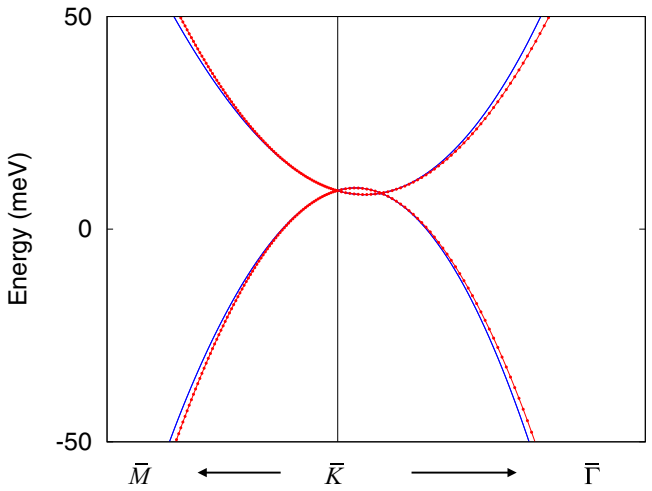

FIG. 14. Comparison between DFT bands and the bands from the $k \cdot p$ model [Eq. (D22)] at $\bar{K}$ point for Ti-terminated surface of TiB_2. Blue lines come from DFT calculations and red dotted lines come from the $k \cdot p$ model.

by

$$D(c_{3z}) = \begin{pmatrix} e^{-2i\pi/3} & 0 \\ 0 & e^{2i\pi/3} \end{pmatrix}, \quad \sigma_v = \begin{pmatrix} 0 & -1 \\ -1 & 0 \end{pmatrix}. \quad \text{(D21)}$$

Considering the above symmetries and the constraint of Eq. (D1), a two-band model up to the second order of k around $\bar{K}$ point for surface states is given by

$$H(\mathbf{k}) = \begin{pmatrix} Bk^2 & Ak_+ + Ck_-^2 \\ Ak_- + Ck_+^2 & Bk^2 \end{pmatrix}, \quad \text{(D22)}$$

TABLE I. Parity of the occupied bands of TiB_2 at TRIMs, Γ_i is in unit of the reciprocal lattice vectors. "Total" means the product of all parities of occupied bands. Γ_0, $\Gamma_1(\Gamma_2)$, Γ_3, and Γ_5 are the same as the notional Γ, M, A, and L, respectively.

TRIM	parity						Total
Γ_0 (0.0, 0.0, 0.0)	+	+	+	−	+		−
Γ_1 (0.5, 0.0, 0.0)	+	−	−	+	+		+
Γ_2 (0.0, 0.5, 0.0)	+	−	−	+	+		+
Γ_3 (0.0, 0.0, 0.5)	−	+	−	−	+	+	−
Γ_4 (0.5, 0.5, 0.0)	+	−	−	+	+		+
Γ_5 (0.0, 0.5, 0.5)	+	−	+	+	−		+
Γ_6 (0.5, 0.0, 0.5)	+	−	+	+	−		+
Γ_7 (0.5, 0.5, 0.5)	+	−	+	+	−		+

where $k_\pm = k_x \pm ik_y$ and $k^2 = k_x^2 + k_y^2$. The linear part of Eq. (D22) leads to massless Dirac dispersion $E(k) = \pm|k|$. The combination of the linear term and the quadratic term leads to threefold rotation symmetry of the energy dispersion. Fitting to the DFT-calculated band structure as shown in Fig. 14, we obtain the following parameters for the Ti-terminated surface, $A = 0.08$ eVÅ, $B = -0.46$ eVÅ^2, $C = 2.3$ eVÅ^2, and for the B-terminated surface, $A = 1.5$ eV Å, $B = 0$, $C = 0$.

APPENDIX E: PARITIES AT TRIMS

The parities of the occupied bands of TiB_2 at TRIMs are listed in Table I. It is noted that there are six occupied bands at A, and five occupied bands at other TRIMs. The product of the parities of the occupied bands at M and L is 1, which leads to $\xi_M = 1$ and $\xi_L = 1$.

[1] C. K. Chiu, J. C. Y. Teo, A. P. Schnyder, and S. Ryu, Rev. Mod. Phys. **88**, 035005 (2016).
[2] T. Bzdušek, Q. Wu, A. Rüegg, M. Sigrist, and A. A. Soluyanov, Nature (London) **538**, 75 (2016).
[3] S. Kobayashi, Y. Yamakawa, Y. Ai, T. Inohara, Y. Okamoto, and Y. Tanaka, Phys. Rev. B **95**, 245208 (2017).
[4] A. A. Burkov, M. D. Hook, and L. Balents, Phys. Rev. B **84**, 235126 (2011).
[5] X. Wan, A. M. Turner, A. Vishwanath, and S. Y. Savrasov, Phys. Rev. B **83**, 205101 (2011).
[6] H. Weng, C. Fang, Z. Fang, B. A. Bernevig, and X. Dai, Phys. Rev. X **5**, 011029 (2015).
[7] S.-M. Huang, S.-Y. Xu, I. Belopolski, C.-C. Lee, G. Chang, B. Wang, N. Alidoust, G. Bian, M. Neupane, C. Zhang, S. Jia, A. Bansil, H. Lin, and M. Z. Hasan, Nat. Commun. **6**, 7373 EP (2015).
[8] S.-Y. Xu, I. Belopolski, N. Alidoust, M. Neupane, G. Bian, C. Zhang, R. Sankar, G. Chang, Z. Yuan, C.-C. Lee, S.-M. Huang, H. Zheng, J. Ma, D. S. Sanchez, B. Wang, A. Bansil, F. Chou, P. P. Shibayev, H. Lin, S. Jia, and M. Z. Hasan, Science **349**, 613 (2015).
[9] B. Q. Lv, H. M. Weng, B. B. Fu, X. P. Wang, H. Miao, J. Ma, P. Richard, X. C. Huang, L. X. Zhao, G. F. Chen, Z. Fang, X. Dai, T. Qian, and H. Ding, Phys. Rev. X **5**, 031013 (2015).
[10] A. A. Soluyanov, D. Gresch, Z. Wang, Q. Wu, M. Troyer, X. Dai, and B. A. Bernevig, Nature (London) **527**, 495 (2015).
[11] K. S. Novoselov, A. K. Geim, S. Morozov, D. Jiang, M. Katsnelson, I. Grigorieva, S. Dubonos, and A. Firsov, Nature (London) **438**, 197 (2005).
[12] Z. Wang, Y. Sun, X. Q. Chen, C. Franchini, G. Xu, H. Weng, X. Dai, and Z. Fang, Phys. Rev. B **85**, 195320 (2012).
[13] Z. K. Liu, B. Zhou, Y. Zhang, Z. J. Wang, H. M. Weng, D. Prabhakaran, S. K. Mo, Z. X. Shen, Z. Fang, X. Dai, Z. Hussain, and Y. L. Chen, Science **343**, 864 (2014).
[14] S. M. Young, S. Zaheer, J. C. Y. Teo, C. L. Kane, E. J. Mele, and A. M. Rappe, Phys. Rev. Lett. **108**, 140405 (2012).
[15] Z. Zhu, G. W. Winkler, Q. S. Wu, J. Li, and A. A. Soluyanov, Phys. Rev. X **6**, 031003 (2016).
[16] H. Weng, C. Fang, Z. Fang, and X. Dai, Phys. Rev. B **93**, 241202 (2016).
[17] G. Chang, S.-Y. Xu, S.-M. Huang, D. S. Sanchez, C.-H. Hsu, G. Bian, Z.-M. Yu, I. Belopolski, N. Alidoust, H. Zheng, T.-R. Chang, H.-T. Jeng, S. A. Yang, T. Neupert, H. Lin, and M. Z. Hasan, Sci. Rep. **7**, 1688 (2017).

[18] B. Bradlyn, J. Cano, Z. Wang, M. G. Vergniory, C. Felser, R. J. Cava, and B. A. Bernevig, Science **353**, aaf5037 (2016).

[19] J. Hu, Z. Tang, J. Liu, X. Liu, Y. Zhu, D. Graf, K. Myhro, S. Tran, C. N. Lau, J. Wei, and Z. Mao, Phys. Rev. Lett. **117**, 016602 (2016).

[20] G. Bian, T. R. Chang, H. Zheng, S. Velury, S. Y. Xu, T. Neupert, C. K. Chiu, S. M. Huang, D. S. Sanchez, I. Belopolski, N. Alidoust, P.-J. Chen, G. Chang, A. Bansil, H. T. Jeng, H. Lin, and M. Z. Hasan, Phys. Rev. B **93**, 121113 (2016).

[21] R. Yu, Q. Wu, Z. Fang, and H. Weng, Phys. Rev. Lett. **119**, 036401 (2017).

[22] Q. F. Liang, J. Zhou, R. Yu, Z. Wang, and H. Weng, Phys. Rev. B **93**, 085427 (2016).

[23] Y. Zhang, Y. W. Tan, H. L. Stormer, and P. Kim, Nature (London) **438**, 201 (2005).

[24] D. T. Son and N. Yamamoto, Phys. Rev. Lett. **109**, 181602 (2012).

[25] Z. Song, J. Zhao, Z. Fang, and X. Dai, Phys. Rev. B **94**, 214306 (2016).

[26] M. M. Vazifeh and M. Franz, Phys. Rev. Lett. **111**, 027201 (2013).

[27] K. Fukushima, D. E. Kharzeev, and H. J. Warringa, Phys. Rev. D **78**, 074033 (2008).

[28] M. N. Ali, J. Xiong, S. Flynn, J. Tao, Q. D. Gibson, L. M. Schoop, T. Liang, N. Haldolaarachchige, M. Hirschberger, N. P. Ong, and R. J. Cava, Nature (London) **514**, 205 (2014).

[29] A. A. Zyuzin and A. A. Burkov, Phys. Rev. B **86**, 115133 (2012).

[30] P. Hosur and X. Qi, C. R. Phys. **14**, 857 (2013).

[31] X. Huang, L. Zhao, Y. Long, P. Wang, D. Chen, Z. Yang, H. Liang, M. Xue, H. Weng, Z. Fang, X. Dai, and G. Chen, Phys. Rev. X **5**, 031023 (2015).

[32] P. Carmier and D. Ullmo, Phys. Rev. B **77**, 245413 (2008).

[33] Z. Yan, R. Bi, H. Shen, L. Lu, S. Zhang, and Z. Wang, Phys. Rev. B **96**, 041103(R) (2017).

[34] C. Fang, H. Weng, X. Dai, and Z. Fang, Chin. Phys. B **25**, 117106 (2016).

[35] R. Yu, Z. Fang, X. Dai, and H. Weng, Frontiers Physics **12**, 127202 (2017).

[36] M. Hirayama, R. Okugawa, T. Miyake, and S. Murakami, Nat. Commun. **8**, 14022 (2017).

[37] Y. Cheng, X. Feng, X. Cao, B. Wen, Q. Wang, Y. Kawazoe, and P. Jena, Small **13**, 1602894 (2017).

[38] Y. Kim, B. J. Wieder, C. L. Kane, and A. M. Rappe, Phys. Rev. Lett. **115**, 036806 (2015).

[39] C. Fang, Y. Chen, H.-Y. Kee, and L. Fu, Phys. Rev. B **92**, 081201 (2015).

[40] T. T. Heikkila and G. E. Volovik, New J. Phys. **17**, 1 (2015).

[41] T. Hyart and T. T. Heikkila, Phys. Rev. B **93**, 235147 (2016).

[42] H. Weng, Y. Liang, Q. Xu, R. Yu, Z. Fang, X. Dai, and Y. Kawazoe, Phys. Rev. B **92**, 045108 (2015).

[43] R. Yu, H. Weng, Z. Fang, X. Dai, and X. Hu, Phys. Rev. Lett. **115**, 036807 (2015).

[44] P. Chang and C. Yee, Phys. Rev. B **96**, 081114 (2017).

[45] W. Chen, H. Lu, and J. Hou, Phys. Rev. B **96**, 041102 (2017).

[46] C. K. Chiu and A. P. Schnyder, Phys. Rev. B **90**, 205136 (2014).

[47] A. Waśkowska, L. Gerward, J. S. Olsen, K. R. Babu, G. Vaitheeswaran, V. Kanchana, A. Svane, V. Filipov, G. Levchenko, and A. Lyaschenko, Acta Mater. **59**, 4886 (2011).

[48] N. L. Okamoto, M. Kusakari, K. Tanaka, H. Inui, and S. Otani, Acta Mater. **58**, 76 (2010).

[49] R. Kumar, M. Mishra, B. Sharma, V. Sharma, J. Lowther, V. Vyas, and G. Sharma, Comput. Mater. Sci. **61**, 150 (2012).

[50] H. Wang, F. Xue, N. H. Zhao, and D. J. Li, in *Advances in Composites*, Advanced Materials Research, Vol. 150 (Trans Tech Publications, 2011), pp. 40–43.

[51] S. Altmann and P. Herzig, *Point-Group Theory Tables*, Oxford Science Publications (Clarendon Press, 1994).

[52] J. M. Cornwall, Phys. Rev. D **59**, 125015 (1999).

[53] B. Post, F. W. Glaser, and D. Moskowitz, Acta Metall. **2**, 20 (1954).

[54] V. Milman and M. C. Warren, J. Phys.: Condens. Matter **13**, 5585 (2001).

[55] See Supplemental Material at http://link.aps.org/supplemental/10.1103/PhysRevMaterials.2.014202 for band character of TiB2 close to the Fermi level.

[56] T. Tanaka and Y. Ishizawa, J. Phys. C: Solid State Phys. **13**, 6671 (1980).

[57] D. Parker, M. G. Vavilov, A. V. Chubukov, and I. I. Mazin, Phys. Rev. B **80**, 100508 (2009).

[58] D. Takane, Z. Wang, S. Souma, K. Nakayama, C. X. Trang, T. Sato, T. Takahashi, and Y. Ando, Phys. Rev. B **94**, 121108 (2016).

[59] Q. Wu, S. Zhang, H.-F. Song, M. Troyer, and A. A. Soluyanov, Comput. Phys. Commun. (2017), doi:10.1016/j.cpc.2017.09.033.

[60] Y. H. Chan, C. Chiu, M. Y. Chou, and A. P. Schnyder, Phys. Rev. B **93**, 205132 (2016).

[61] M. P. L. Sancho, J. M. L. Sancho, J. M. L. Sancho, and J. Rubio, J. Phys. F: Met. Phys. **15**, 851 (1985).

[62] L. Z. Zhang, Z. F. Wang, S. X. Du, H. J. Gao, and F. Liu, Phys. Rev. B **90**, 161402 (2014).

[63] X. Zhang, Z. Yu, X. Sheng, H. Y. Yang, and S. A. Yang, Phys. Rev. B **95**, 235116 (2017).

[64] P. Hohenberg and W. Kohn, Phys. Rev. **136**, B864 (1964).

[65] W. Kohn and L. J. Sham, Phys. Rev. **140**, A1133 (1965).

[66] G. Kresse and J. Furthmüller, Comput. Mater. Sci. **6**, 15 (1996).

[67] G. Kresse and J. Furthmüller, Phys. Rev. B **54**, 11169 (1996).

[68] G. Kresse and D. Joubert, Phys. Rev. B **59**, 1758 (1999).

[69] P. E. Blöchl, Phys. Rev. B **50**, 17953 (1994).

[70] J. P. Perdew, K. Burke, and M. Ernzerhof, Phys. Rev. Lett. **77**, 3865 (1996).

[71] A. A. Mostofi, J. R. Yates, Y. S. Lee, I. Souza, D. Vanderbilt, and N. Marzari, Comput. Phys. Commun. **178**, 685 (2008).

[72] D. Gresch, Q. Wu, G. W. Winkler, and A. A. Soluyanov, New J. Phys. **19**, 035001 (2017).

[73] G. F. Koster, *Properties of Thirty-Two Point Groups* (MIT Press, Cambridge, MA, 1962).